

Predicting Cell Stress and Strain during Extrusion Bioprinting

Sebastian J. Müller^{1,*}, Ben Fabry², and Stephan Gekle^{1,†}

¹*Biofluid Simulation and Modeling, Theoretische Physik VI, Universität Bayreuth, Bayreuth 95440, Germany*

²*Department of Physics, Friedrich-Alexander University Erlangen-Nürnberg, Erlangen 91054, Germany*

 (Received 30 September 2022; revised 28 December 2022; accepted 1 May 2023; published 21 June 2023)

Bioprinting of living cells can cause major shape deformations, which may severely affect cell survival and functionality. While the shear stresses occurring during cell flow through the printer nozzle have been quantified to some extent, the extensional stresses occurring as cells leave the nozzle into the free printing strand have been mostly ignored. Here we use lattice Boltzmann simulations together with a finite-element based cell model to study cell deformation inside the nozzle and at its exit. Our simulation results are in good qualitative agreement with experimental microscopy images. We show that, for cells flowing in the center of the nozzle, extensional stresses can be significant while, for cells flowing off-center, their deformation is dominated by the shear flow inside the nozzle. From the results of these simulations, we develop two simple methods that only require the printing parameters (nozzle diameter, flow rate, bioink rheology) to (i) accurately predict the maximum cell stress occurring during the three-dimensional bioprinting process and (ii) approximately predict the cell strains caused by the elongational flow at the nozzle exit.

DOI: [10.1103/PhysRevApplied.19.064061](https://doi.org/10.1103/PhysRevApplied.19.064061)

I. INTRODUCTION

The aim of three-dimensional (3D) bioprinting is to transfer the well-established techniques of conventional 3D printing to the fabrication of functional, living tissues. The material to be printed typically consists of a chemically complex hydrogel, termed the bioink, in which living cells are suspended. This technology promises to become a major breakthrough, e.g., for cancer studies or—in the long run—organ replacements [1–5]. A key obstacle, however, remains to ensure the survival and functionality of cells during and after the fabrication process. Possible causes for cell damage are numerous, but can be broadly classified into insufficient bio-compatibility and mechanical damage. The former arises from direct interaction between the cell and the surrounding bioink and has been intensively studied [6–13].

Mechanical damage, by contrast, arises from hydrodynamic stresses as the cell passes from the reservoir through the printing nozzle, transitions into the printing strand, and finally comes to rest in the printed construct.

It has been shown that even after optimizing biological and chemical conditions [14], such hydrodynamic stresses remain a crucial source of cell damage and death [15–25]. Understanding these mechanical stress response processes is notoriously difficult as they result from an interplay between the complex rheology of the bioink, which is typically shear thinning [26–29], and the even more complex viscoelastic response of the cell itself [30–40]. Despite these difficulties, certain progress towards reliable theoretical estimates of the cell stress inside printing needles has been achieved [15,18,41]. As a starting point, the fluid shear stress profiles within printing nozzles have been computed theoretically [17,21,42]. Some experimental studies correlated such stress calculations with cell viability or functionality [15,22,41,43–48]. These studies, however, investigated hydrodynamic stresses only up to the end of the printing nozzle. At the transition from the nozzle exit into the free strand, the flow profile transitions rapidly from a Poiseuille-like profile in the nozzle to a plug-flow profile inside the free bioink strand. This transition is accompanied by sizable radial flows whose effect on cell deformation and, therefore, cell damage has so far not been experimentally or theoretically quantified.

In this work we start with fully three-dimensional lattice Boltzmann calculations for the flow profile of shear thinning fluids [42] at the exit of a printing nozzle. To investigate cell stress and strains inside and during exit from the printing nozzle, we employ our recently developed hyperelastic cell model [31] that includes explicit

*sjmueller@uni-bayreuth.de

†www.gekle.physik.uni-bayreuth.de

Published by the American Physical Society under the terms of the [Creative Commons Attribution 4.0 International](https://creativecommons.org/licenses/by/4.0/) license. Further distribution of this work must maintain attribution to the author(s) and the published article's title, journal citation, and DOI.

two-way coupling between bioink and cellular mechanics, and show its qualitative match with experimental micrographs taken during the printing process. From these investigations we develop simple methods to predict the cell stress and strains occurring during bioprinting processes, and specifically during nozzle exit, by only using the printing parameters, i.e., the nozzle diameter, the bioink rheology, and the volumetric flow rate, as input quantities. For this, we combine the classical theories of Jeffery [49] and Roscoe [50] with our semi-analytical flow computations of shear thinning bioinks in capillaries [42].

II. METHODS AND SETUP

A. Flow dynamics: lattice Boltzmann simulations

In our simulations we employ a fully three-dimensional fluid dynamics solver. We use the implementation of the lattice Boltzmann method [51,52] provided by the software package ESPRESSO [53,54], which we extended with algorithms to allow for the simulation of free-slip surfaces [55] and shear thinning fluids [42]. Using an immersed-boundary algorithm [33,56–58], we couple our cell model (Sec. II C) to the flow.

B. Bioink rheology

The shear thinning rheology is considered an essential material property for bioinks, as it serves two purposes. First, the large viscosity of the material at rest provides the necessary mechanical stability of the printed construct itself. Second, the shear thinning properties allow the material to be printed at significantly lower pressure—considering the same printing speed—thus reducing the overall hydrodynamic stresses acting on cells inside the nozzle.

We describe the viscosity as a function of the rate of strain $|\dot{S}|$ according to a three-parameter simplified Carreau-Yasuda model, also known as the Cross model [42,59],

$$\eta(|\dot{S}|) = \frac{\eta_0}{1 + (K|\dot{S}|)^\alpha}. \quad (1)$$

Here, η_0 is the zero-shear viscosity and the exponent α characterizes the shear thinning strength of the bioink, with $\alpha = 0$ for a Newtonian fluid and $\alpha > 0$ for a shear thinning fluid. The inverse of the time constant, K^{-1} , defines the rate of strain at which the viscosity is equal to $\eta_0/2$. Here $|\dot{S}|$ is calculated as the contraction of the rate of strain tensor \dot{S} via

$$|\dot{S}| = \sqrt{2\dot{S}_{ij}\dot{S}_{ij}}, \quad (2)$$

with the tensor elements

$$\dot{S}_{ij} = \frac{1}{2} \left(\frac{\partial u_i}{\partial x_j} + \frac{\partial u_j}{\partial x_i} \right). \quad (3)$$

The diagonal elements of \dot{S} are the rates of elongation of the fluid along the coordinate axes, and the off-diagonal elements are the respective shear rates. We choose $\eta_0 = 10$ Pa s and $K = 0.05$ s for the zero-shear viscosity and time constant, respectively. This parameter choice roughly resembles the values obtained for 2.5% alginate hydrogels [26,42,60], which is a widely used bioink material, although other materials can exhibit similar shear thinning properties. In order to investigate the influence of the shear thinning strength in our calculations, we pick six different values for α between 0 and 1 with $\alpha = 0.75$ [42] corresponding to the said alginate solution. The viscosity as a function of the shear rate is depicted in Fig. 1(a). For an idealized, i.e., infinitely long, cylindrical nozzle, the velocity profile and the fluid stress σ_f can be computed according to Refs. [42,61] as shown in Figs. 1(b) and 1(c) with the pressure adjusted so as to ensure the same flow rate for each α . In our previous study [42] we introduced this method to calculate the velocity, shear rate, viscosity, and shear stress profiles for an inelastic shear thinning fluid in a cylindrical nozzle. The central assumptions—a laminar, uniaxial, pressure driven, flow—are usually applicable for the description of bioink extrusion. In the following we define the fluid stress as

$$\sigma_f = \eta(|\dot{S}|)|\dot{S}|. \quad (4)$$

We note that, if a constant extrusion pressure is used for the calculation, the fluid stress profile in Fig. 1(c) is the same regardless of α [42].

C. Cell elasticity

1. Hyperelastic cell model

Our cell is modeled as a hyperelastic continuum, with a sphere as the equilibrium configuration. We provide extensive validation of the model in a previous publication [31]. This includes atomic force microscopy (AFM) and FluidFM[®] measurements on biological cells and hydrogel particles as well as comparison to analytical theories [39,50] and previous numerical simulations in shear flow [33,62].

As a hyperelastic model, we employ the neo-Hookean material model. This model is strain hardening for compressive strain, e.g., in AFM experiments, but also for shear strains as occurring mainly in microfluidic experiments. Its strain-energy density is computed via [63, p. 100]

$$U = \frac{\mu}{2} (I - 1) + \frac{\kappa}{2} (J - 1)^2, \quad (5)$$

where $J = \det(F)$ is the determinant of the deformation gradient tensor $F_{ij} = \partial x_i / \partial y_j$ [63, p. 14, 18], with the undeformed and deformed vertex coordinates x_i and y_i , respectively. Here $I = J^{-2/3} \text{tr}(F^T F)$ denotes the second

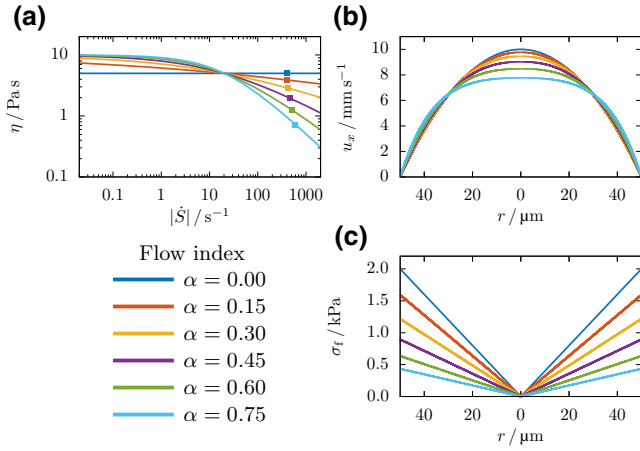


FIG. 1. (a) Viscosity as a function of the shear rate for the six different degrees of shear thinning ($\alpha = 0, 0.15, 0.3, 0.45, 0.6, \text{ and } 0.75$). Squares indicate the maximum shear rate in the nozzle channel under the flow conditions used in our simulations (cf. Sec. II D). (b) Corresponding velocity profiles for an average velocity of 5 mm s^{-1} inside the cylindrical printing nozzle. With increasing shear thinning strength, the velocity profile flattens at the center. (c) Corresponding fluid stress profiles. Stresses are linear with the radial position, and the maximum fluid stress decreases significantly with increasing α at constant flow rate.

invariant of F . For the elastic parameters, we choose a shear modulus of $\mu = 1000 \text{ Pa}$ and a Poisson ratio of $\nu = 0.48$. A simulation series with $\mu = 500 \text{ Pa}$ is included in Sec. S9 of the Supplementary Material [64]. The Poisson ratio near 0.5 provides sufficient incompressibility of the cell, while the shear modulus lies in the range typically found for mammalian stem cells [65]. Consistent with the linear elasticity of small deformations, the shear and bulk modulus relate to the Young's modulus and Poisson ratio via

$$\mu = \frac{E}{2(1+\nu)} \quad \text{and} \quad \kappa = \frac{E}{3(1-2\nu)}. \quad (6)$$

The cell radius is chosen as $R_c = 8 \text{ } \mu\text{m}$ (6 in simulation units), and the mesh consists of 9376 tetrahedra.

In our numerical method the interior of the cell is filled with the same fluid as the outside fluid. Together with the Neo-Hookean elasticity, this leads to an effectively viscoelastic cell response [31].

2. Force calculation and flow coupling

For numerical simulations, the spherical volume is uniformly tetrahedralized using the meshing software GMSH [66]. The elastic forces acting on each vertex of one tetrahedron are obtained via differentiation of the strain-energy density (5) with respect to the relative vertex displacement,

$$f_i = -V_0 \frac{\partial U}{\partial u_i}, \quad (7)$$

where V_0 denotes the reference volume of the tetrahedron and $u_i = y_i - x_i$. This approach is explained in detail in Sec. 3.1 in Ref. [31].

The coupling between the cell model and the bioink is realized using an immersed-boundary algorithm [67,68]. After computation of the cell vertex forces, they are transmitted into the fluid via extrapolation from the moving Lagrangian cell mesh onto the static Eulerian lattice Boltzmann grid. The two-way coupling is completed through advecting the cell vertices with the local interpolated fluid velocity.

3. Cell stress calculations

In addition to the elastic forces, we are able to obtain the internal stress distribution inside our cell model. We compute the Cauchy stress tensor in each tetrahedron from the strain-energy density and the deformation gradient tensor according to Bower [63, p. 97] as

$$\sigma_{ij} = J^{-1} F_{ik} \frac{\partial U}{\partial F_{jk}}. \quad (8)$$

For the neo-Hookean model in Eq. (5), this becomes

$$\sigma_{ij} = \frac{\mu}{J^{5/3}} \left(B_{ij} - \frac{1}{3} B_{kk} \delta_{ij} \right) + \kappa (J - 1) \delta_{ij}, \quad (9)$$

where $B = FF^T$ denotes the left Cauchy-Green deformation tensor.

In order to obtain a simple scalar observable to quantify the cell stress, we start from the local von Mises stress in each tetrahedron. The von Mises stress is an invariant of the Cauchy stress tensor and commonly used in plasticity theory to predict yielding of materials under multiaxial loading conditions through construction of a fictitious uniaxial loading. Using the principal stresses, i.e., the eigenvalues $\sigma_1, \sigma_2,$ and σ_3 , of the Cauchy stress tensor, Eq. (9), we calculate [63, p. 48]

$$\sigma_{\text{vM}} = \sqrt{\frac{1}{2} [(\sigma_1 - \sigma_2)^2 + (\sigma_2 - \sigma_3)^2 + (\sigma_3 - \sigma_1)^2]}. \quad (10)$$

An alternative equivalent formulation to Eq. (10) is the contraction of the deviator of the Cauchy stress tensor $\sigma_{ij}^{\text{dev}} = \sigma_{ij} - \frac{1}{3} \sigma_{kk} \delta_{ij}$. It reads

$$\sigma_{\text{vM}} = \sqrt{\frac{3}{2} \sigma_{ij}^{\text{dev}} \sigma_{ij}^{\text{dev}}}. \quad (11)$$

The total cell stress σ_{vM} is then computed by averaging the local von Mises stress over all tetrahedra in the cell model weighted by the undeformed volume of each tetrahedron.

4. Validation of the cell stress calculation

We validate our cell stress calculations using a linear shear flow setup: the simulation box with dimensions $10 \times 15 \times 5$ ($x \times y \times z$ in units of R_c) is bounded by two planes at $y = 0$ and $y = 15R_c$, moving with a tangential velocity in the $\pm x$ direction. This creates a linearly increasing velocity across the gap and, thus, a constant shear rate $\dot{\gamma}$ in the box. The shear rate is varied to achieve a range of fluid stresses up to 1.5 kPa, while the fluid viscosity ($\alpha = 0$) and the cell's shear modulus remain constant. In non-dimensional terms this range corresponds to capillary numbers $Ca = \sigma_f / \mu$ between 0 and 1.5.

During the simulation, the initially spherical cell traverses through a series of ellipsoidal deformations before reaching a stationary state, at which point the whole cell volume performs a tank-treading motion, i.e., the cell vertices rotate around the fixed ellipsoidal cell shape. In Fig. 2 we compare the elastic cell stress in the stationary state calculated by Eq. (10) to the analytical calculations of Roscoe [50] (detailed in Sec. S4 of the Supplementary Material [64]) and find excellent agreement for a realistic range of fluid stresses.

In addition to the elastic stress, we compute the viscous contribution resulting from the fluid motion enclosed by the cell volume. This quantity is extracted from the lattice Boltzmann strain rate tensor field [42,69] inside the cell using our method from Ref. [70] and averaging over the cell volume. In Fig. S-2 of the Supplementary Material [64] we show that the agreement of the numerically obtained viscous cell stress with Roscoe theory is equally as good as for the elastic component.

We note that the cell and fluid stresses in Fig. 2 are time independent and stationary. We further dissect their relation in detail in Sec. III A.

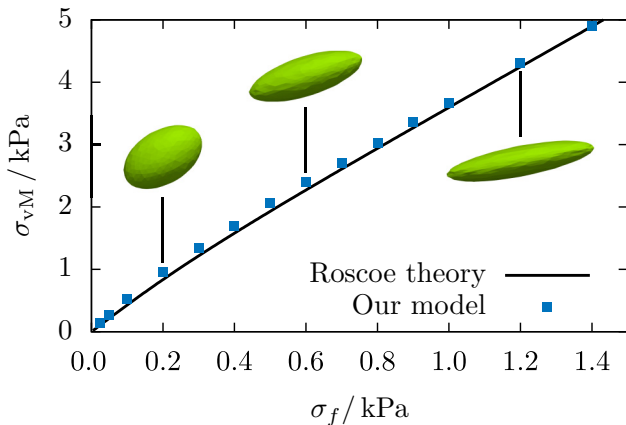


FIG. 2. Comparison of the cell stress predicted by Roscoe [50] and the average cell stress of our model in shear flow. Insets show the stationary, tank-treading shape of the simulated cell at fluid stresses corresponding to $Ca = 0.2, 0.6,$ and 1.2 .

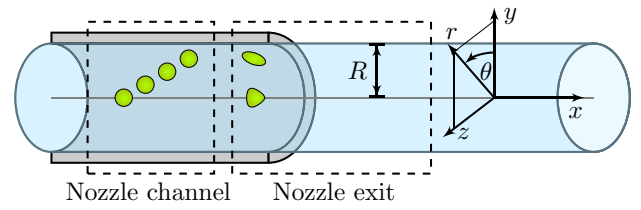


FIG. 3. Schematic of the bioprinter setup: the nozzle channel is bounded by a cylindrical wall and periodic in the x direction. Single cells are inserted at different radial offsets. The nozzle exit consists of the transition from the no-slip nozzle channel to the free bioink strand. Cells are initialized in a deformed state close to the transition.

D. Bioprinting simulations

The two essential parts of the bioprinting process are (i) the flow inside the nozzle channel and (ii) the flow transition at the nozzle exit. Both situations are studied separately in this work.

1. Nozzle channel

We model the nozzle channel using a periodic cylindrical no-slip channel with a radius of $R = 50 \mu\text{m}$ and length of $133 \mu\text{m}$ (37.5 and 100 in simulation units), as depicted in the left dashed box in Fig. 3. The shear thinning fluid dynamics are solved by the lattice Boltzmann method as described in Sec. II A. No-slip boundary conditions are imposed at the channel wall. The flow is driven by a pressure gradient G along the nozzle axis. To compare the different bioinks detailed in Sec. II B, we consider a fixed average velocity of 5 mm s^{-1} (volumetric flow rate $\Omega = 3.93 \times 10^{-11} \text{ m}^3 \text{ s}^{-1} \approx 141 \mu\text{l h}^{-1}$). The corresponding pressure gradient is different for each α and is obtained according to Ref. [42]. Our input parameters as well as the averaged and maximum quantities of the nozzle channel flow are listed in Table I. We note that compared with common flow cytometry setups [32,36], the channel radius in typical bioprinting applications is significantly larger, thus allowing cells to flow off-centered. To account for this, a single spherical cell is inserted at different radial starting positions of $0, 1.5 R_c, 3 R_c,$ and $4.5 R_c$, as shown in Fig. 3.

TABLE I. Flow parameters of our bioprinter setup with a nozzle radius of $50 \mu\text{m}$ and an average velocity of 5 mm s^{-1} .

α	G Pa m^{-1}	σ_f^{max} kPa	σ_f^{avg} kPa	u_x^{max} mm s^{-1}	$ \dot{S} ^{\text{max}}$ s^{-1}	$ \dot{S} ^{\text{avg}}$ s^{-1}
0.00	8.00×10^7	2.00	1.33	10.0	400	267
0.15	6.37×10^7	1.59	1.06	9.77	410	265
0.30	4.87×10^7	1.22	0.81	9.45	426	262
0.45	3.58×10^7	0.89	0.60	9.03	454	257
0.60	2.54×10^7	0.63	0.42	8.47	502	251
0.75	1.74×10^7	0.44	0.29	7.77	604	242

2. Nozzle exit

The geometry of our simulations at the nozzle exit is depicted by the right dashed box in Fig. 3, the flow dynamics are again solved by the lattice Boltzmann method. The free bioink strand of length $933 \mu\text{m}$ (700 in simulation units) behind the nozzle exit is assumed to have the same radius as the inner radius of the nozzle channel, with free-slip boundary conditions applied at the fluid surface, which result in a plug motion of the bioink. This way we neglect the small extension of the bioink strand at the nozzle exit known as the Barus effect or die swell [71]. Equal flow conditions as inside the nozzle channel are achieved by applying the average velocity of 5 mm s^{-1} as normal velocity at the circular inflow and outflow planes, instead of a constant pressure gradient as used in the nozzle channel setup. We insert a single cell at different radial positions as explained above. The starting configuration of the cell is taken from the corresponding simulation of the nozzle channel setup, i.e., the cell is inserted in a deformed state close to the nozzle exit, as shown in the first frames of Fig. 9.

III. RESULTS

A. Dissecting the notion of “cell stress”

In many situations it has become a common approach to invoke the term “cell stress” and to equate it directly to the fluid stress, i.e., the viscosity multiplied by the local shear rate at the cell position. Here, we show that this simple approach, while being correct in its order of magnitude, hides a good amount of the more complex features of intracellular stress. To illustrate this, we apply the theory of Roscoe [50] for a cell in linear shear flow, which accurately describes cell behavior in our numerical simulations (see Sec. II C 4) and in microchannel experiments [72], provided that the cell does not flow in the channel center where the shear rate approaches zero.

Inside a flowing cell, two qualitatively different kinds of stress arise. The first kind are viscous stresses that are caused by frictional motion (i.e., tank treading) of the cell interior. The second kind are elastic stresses that are caused by the deformation (e.g., shearing and stretching) of the cell. The magnitude of the former are governed by the cell’s internal viscosity, while the latter are set by its elastic moduli. We note that, in principle, both a cell’s viscosity and its elasticity can be nonhomogeneous, i.e., they vary spatially throughout the cell, and anisotropic, i.e., they depend on direction, e.g., due to alignment of certain cytoskeletal elements. Here and in most other situations, these more complicated effects are neglected, and the cell is considered a homogeneous, isotropic viscoelastic medium. Furthermore, as shown in Ref. [50] for a cell

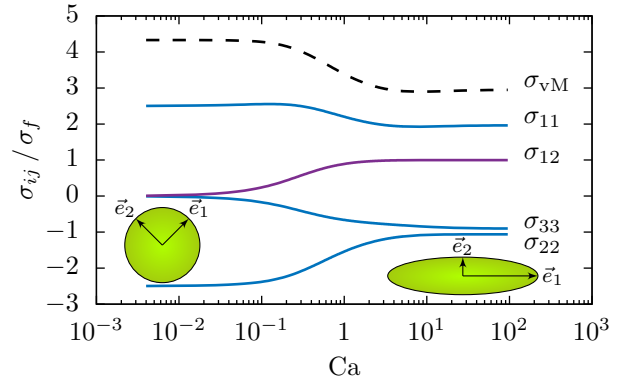


FIG. 4. Components of the cell stress tensor σ_{ij} normalized by the undisturbed fluid stress σ_f across multiple orders of magnitude of the capillary number computed using the Roscoe theory. Elastic stresses are shown in blue, viscous stresses are shown in purple. Components not appearing in the figure remain zero throughout. The directions 1, 2, 3 refer to a body-fixed coordinate system as indicated by the insets.

in pure shear flow, stability requires that viscous and elastic cellular stresses do not vary between different locations inside the cell. Their value can be calculated from Roscoe theory as detailed in the Supplementary Material [64], see Eqs. (S-43) and (S-48).

We start with the limiting case of low shear rates corresponding to small capillary numbers $Ca = \sigma_f / \mu \rightarrow 0$. In this limit, fluid stresses are not sufficient to cause significant cell deformation, and the cell essentially remains spherical. Indeed, the classical calculation for a rigid sphere in shear flow detailed in Sec. S6 of the Supplementary Material [64] yields a surprisingly accurate description of this limit. The cell rotates as a rigid body, which implies the absence of internal frictional motions and, thus, leads to a vanishing viscous cell stress as shown by the purple curve in Fig. 4. Similarly, elastic stresses in the vorticity direction vanish as shown by the σ_{33} component in Fig. 4. A positive stress appears in a direction inclined by 45° with respect to the flow direction (σ_{11}), with a corresponding negative stress in the perpendicular direction. Their magnitude is precisely $5/2$ times the undisturbed fluid stress σ_f , which exactly corresponds to the situation of the rigid sphere as shown in Sec. S6 of the Supplementary Material [64].

In the opposite limit of high shear rates ($Ca \rightarrow \infty$), the situation becomes more involved. In agreement with our numerical simulations shown in Fig. 2, the cell becomes strongly elongated and aligned in the flow direction. Because of the persisting tank-treading motion, internal viscous stresses do not disappear. Instead, the flatness of the cell shape minimizes the cell’s disturbing influence on the surrounding fluid flow, and indeed the cell’s internal viscous stress now becomes equal to the undisturbed fluid stress, as can be seen by the purple curve in Fig. 4.

Maintaining the flattened cell shape, however, in addition requires elastic stresses. As shown by the blue curve in Fig. 4, all three elastic stress components arise with their ratios being $\sigma_{11} : \sigma_{22} : \sigma_{33} = 2 : -1 : -1$. The positive stress in flow direction, σ_{11} is balanced by negative stresses in the two other directions. These ratios can easily be understood by the analogy with a uniaxially stretched beam as detailed in Sec. S7 of the Supplementary Material [64].

Despite this complexity, it may be helpful in many situations to have at hand a single measure to quantify “cell stress.” Such a measure can be provided by the elastic von Mises stress σ_{vM} given in Eq. (11) that we include as the black dashed line in Fig. 4. The ratio $\sigma_{\text{vM}}/\sigma_f$ transitions from $\frac{5}{2}\sqrt{3}$ at low Ca to 3 at high Ca . In the intermediate range, the proportionality factor is situated between these two limits. As can also be deduced from Fig. 2, the relation between σ_{vM} and σ_f changes the most in the range of $0.1 < \text{Ca} < 1$, while otherwise an approximately linear dependency emerges.

From the results of this subsection, we conclude that the common approach of equating (undisturbed) fluid stress to “cell stress” can be a reasonable approximation for low and high capillary numbers.

B. Cell flowing inside the nozzle channel

Using our setup described in Sec. IID 1, we investigate the cell behavior and the cell’s internal stress distribution during the flow inside the nozzle. Depending on the initial radial position, we observe two modes of deformation of the cell.

(i) A cell flowing along the axis of the nozzle channel assumes an axisymmetric bulletlike shape, as can be seen in Figs. 5(a) and 5(b) for a Newtonian and a highly shear thinning bioink, respectively. In both cases, the radial dependency of the internal cell stress is highly nonhomogeneous and resembles the linearly increasing fluid stress of the undisturbed liquid [cf. Fig. 1(c)], since the cell’s surface has to balance higher fluid shear stresses for increasing r in the stationary state. However, the magnitude of the stress and likewise the cell deformation decrease significantly when the shear thinning index α is increased at the same volumetric flow rate. This finding may explain earlier experimental observations in which more shear thinning bioinks were found to increase cell survival in bioprinting [22,45] when the pressure was reduced to ensure equal flow rates for all conditions.

(ii) A cell flowing off-center deforms into an approximately ellipsoidal shape exhibiting tank-treading motion. Because of the curvature of the flow, the cell migrates towards the channel center, where it eventually assumes the bulletlike shape discussed in the previous paragraph. A sequence of simulation snapshots for a cell flowing in the Newtonian bioink is shown in Fig. 5(c), where the internal

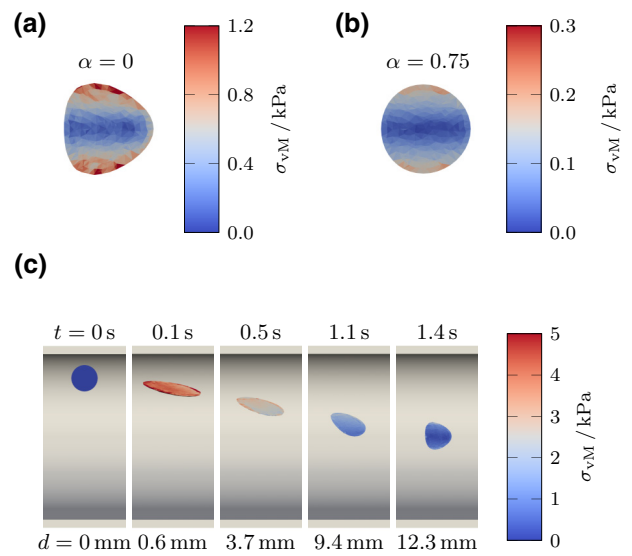


FIG. 5. Internal stress distribution for a cell flowing at the center of the nozzle channel in (a) a Newtonian fluid and (b) a strongly shear thinning fluid. (c) Internal stress distribution and radial migration of an off-centered cell towards the axis of the nozzle channel in a Newtonian bioink. The bottom labels give the axial distance traveled during the time given by the top labels.

stress distribution of the off-centered cells can be observed. Figure 6(a) shows the corresponding development of the radial position over time starting from an offset of $36 \mu\text{m}$. With increasing shear thinning strength, i.e., decreasing pressure gradient, the cell takes longer to migrate towards the channel center.

In Fig. 6(b) the same situation is studied for a constant pressure gradient. We find that here the migration speed of the cell becomes independent of the shear thinning properties of the bioink and, thus, conclude that cell migration is determined predominantly by the applied pressure gradient and not the flow speed. This finding can be understood since the stress, and, thus, the forces, that the cell feels are directly determined by the local fluid stress. Therefore, for printing bioinks with different rheology at the same printing pressure, the radial cell distribution will not change. For printing bioinks with an increasing shear thinning strength at the same flow rate, by contrast, fewer cells migrate to the center of the nozzle.

The ellipsoidal cell shape during the migration allows us to compare the cell stress to the prediction of the Roscoe theory [50] detailed in Sec. IIC 4. In Fig. 6(c) we plot the development of the cell stress in a Newtonian bioink when cells are initially placed at different offsets from the nozzle center. Because of the migration of the cells towards the channel center, the local fluid stress experienced by a given cell decreases monotonically over time. In order to directly compare with the prediction of Roscoe theory, which assumes a constant fluid shear stress, we

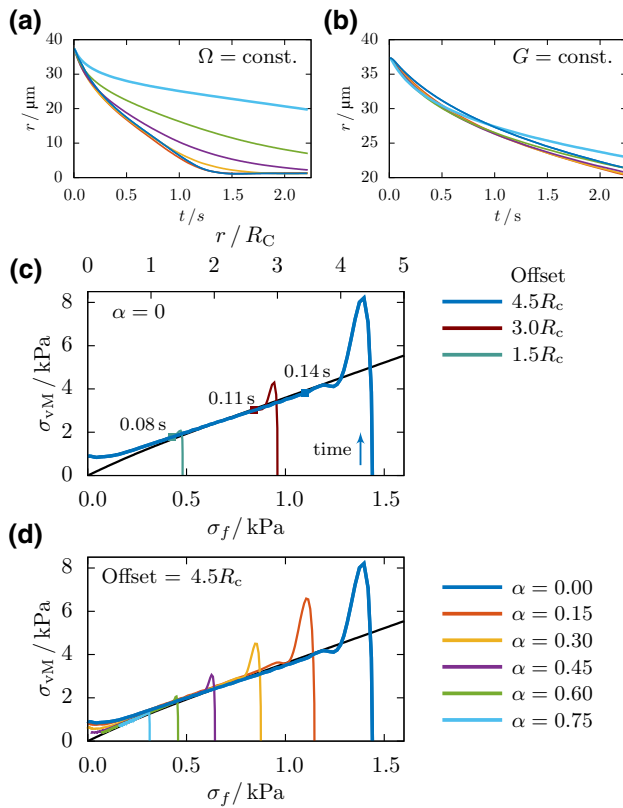


FIG. 6. Radial migration r (center of mass) of a cell starting near the nozzle wall for different shear thinning strengths (see (d) for color labels) with (a) constant flow rate and (b) constant pressure gradient ($G = 1.14 \times 10^7 \text{ Pa m}^{-1}$). For constant G , the migration speed is almost independent of α . (c),(d) Cell stress as a function of the local fluid stress compared with the Roscoe theory (black line). Because of the radial migration of the cell, the cell experiences a continuous change of the local fluid stress over time. (c) The cell starting at different offsets (from right to left: $4.5R_c$, $3R_c$, and $1.5R_c$) in the Newtonian fluid. The duration of the deformation from the spherical reference shape to the approximately elliptical shape is given by the points. (d) Cells starting at offset $4.5R_c$ for bioinks with increasing shear thinning strength in comparison with the Roscoe theory. For details, see text.

choose this local fluid stress as abscissa. Cells start at offsets of 12, 24, and 36 μm corresponding to initial fluid stresses of $\sigma_f \approx 0.5, 1.0, \text{ and } 1.5 \text{ kPa}$, respectively. The initial shape is undeformed and, thus, $\sigma_{vM} = 0$ for $t = 0$. The cell first experiences a transient of large stresses and quickly relaxes towards the cell stress predicted by Roscoe where the curved flow is locally approximated as a pure shear flow, as indicated by the square symbols. Because of the migration towards the channel center, the cell stress decreases with time and radial position. The curves of all initial radial offsets perfectly agree with the prediction of the Roscoe theory, as long as the cell's radial position is larger than R_c . When the cell is close to the channel center,

the local shear flow approximation becomes invalid, thus causing deviations from the theoretical prediction.

A similar plot is provided for shear thinning bioinks in Fig. 6(d) where the stress of cells starting at offset $4.5R_c$ for different α is compared with Roscoe theory. We again find excellent agreement with the Roscoe theory independent of the shear thinning strength. This finding may seem surprising at first, as the theory of Roscoe is designed for purely Newtonian fluids surrounding the cell, but stays valid for shear thinning bioinks as well. This demonstrates that the key property determining cell motion is indeed not the shear rate, but rather the shear stress. The plots for the remaining cell offsets and bioinks are included in the Supplementary Material [64] (cf. Fig. S-3).

C. Analysis of the flow field at the nozzle exit

In this section we investigate the influence of the shear thinning rheology of the bioinks introduced in Sec. II B on the undisturbed (cell free) flow field at the nozzle exit, where the transition from nozzle channel to the free bioink strand causes additional radial flows. We use the second setup described in Sec. II D, without a cell, and run the calculations until the flow becomes stationary.

In Figs. 7(a) and 7(b) we show x - y slices of the velocity profiles for the axial and radial velocity, respectively, at different values of the shear thinning parameter α . From top to bottom, the shear thinning strength of the fluid increases, while the flow rate is kept constant. The axial velocity component in Fig. 7(a) shows the same trend for increasing α as seen in Fig. 1(b): the flow develops a central plateau inside the nozzle channel that at the nozzle exit transitions into the plug flow inside the bioink strand. Indeed, as shown in Fig. 7(c), the ratio $u_x^{\text{max}}/u_x^{\text{avg}}$ between the maximum velocity inside the nozzle channel and the average velocity assumes the Poiseuille value of 2 at $\alpha = 0$ and decreases towards the plug-flow value of 1 for increasing shear thinning strength.

The second column, Fig. 7(b), shows the corresponding radial flow components. Because of the radial symmetry, they vanish at the center and increase towards the boundary, showing a droplike shape with its tip pointing to the position of the nozzle orifice, where the boundary conditions change. The radial flow components decrease with increasing α , since the fluid has to be displaced less due to a smaller axial velocity difference across the transition. Figure 7(d) quantifies this observation by comparison of the maximum radial flow velocity at the exit with the average axial flow.

Combining the axial and radial flows, streamlines are computed in order to visualize the fluid motion in the stationary state. As can be seen in the overlaying lines in Figs. 7(a) and 7(b), the streamlines show very similar elongational behavior for all α at the nozzle exit due to the

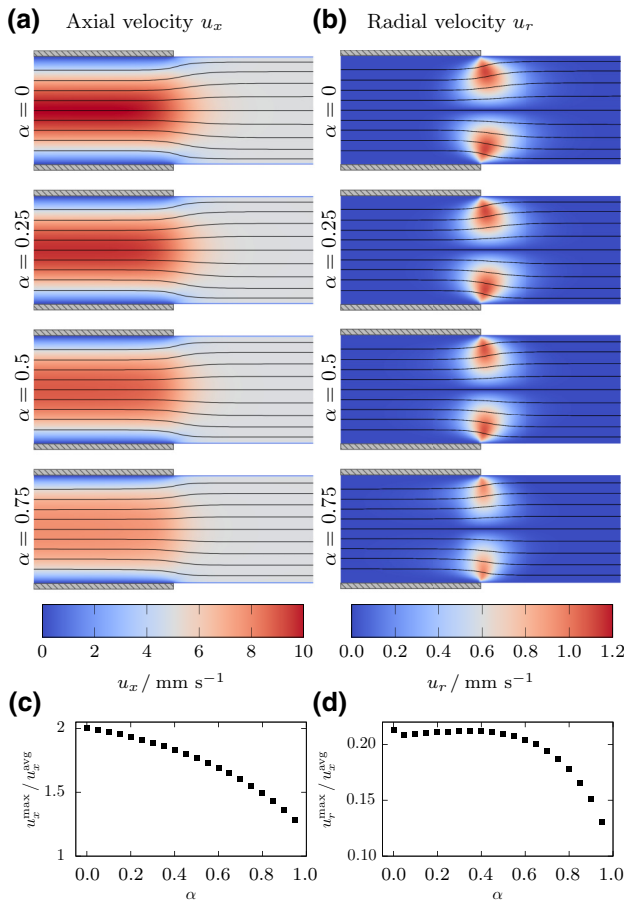


FIG. 7. The x - y slices of the flow at the nozzle exit for increasingly shear thinning fluids: (a) axial velocity component and (b) radial velocity component with streamlines as overlay. (c) The ratio of maximum axial velocity inside the nozzle to the average flow velocity as a function of the shear thinning strength α . (d) The ratio of maximum radial velocity after the nozzle exit to the average flow velocity as a function of α .

simultaneous decrease of the axial and radial flow components. They are, however, not exactly equal, since the maximum axial and radial velocities scale slightly differently with α . Finally, comparing the ratio of axial and radial velocities, we find that the maximum radial flow velocity is always about 10% of the maximum axial flow velocity, roughly independent of α .

The fluid stress along the axial direction for different offsets is shown in Fig. 8 for $\alpha = 0$ and $\alpha = 0.75$. In addition to the total fluid stress, we plot the shear and elongational component separately. To do so, we first decompose the rate of strain tensor into the shear and elongational components [73],

$$\dot{S}_{ij} = \dot{S}_{ij}^{\text{shear}} + \dot{S}_{ij}^{\text{elong}}, \quad (12)$$

where \dot{S}^{elong} is a diagonal tensor and \dot{S}^{shear} contains only off-diagonal elements. Using this decomposition—further

details can be found in Sec. S3 of the Supplementary Material [64]—we can define the shear and elongational components of the fluid stress as

$$\sigma_f^{\text{shear}} := \eta (|\dot{S}|) \sqrt{4\dot{S}_{xr}^2} \quad (13)$$

and

$$\sigma_f^{\text{elong}} := \eta (|\dot{S}|) \sqrt{2(\dot{S}_{xx}^2 + \dot{S}_{rr}^2 + \dot{S}_{\theta\theta}^2)}. \quad (14)$$

Note that $\dot{S}_{x\theta} = \dot{S}_{r\theta} = 0$, since no azimuthal flow components are present, but that nevertheless $\dot{S}_{\theta\theta} \neq 0$ as detailed in Sec. S3 of the Supplementary Material [64]. Thus, the total fluid stress is obtained from Eqs. (13) and (14) via

$$\sigma_f = \sqrt{(\sigma_f^{\text{shear}})^2 + (\sigma_f^{\text{elong}})^2}. \quad (15)$$

Along the channel center [cf. Figs. 8(a) and 8(e)], all shear components of the stress vanish, leaving only the elongational ones, which show a clear peak at the exit. Considering the symmetry, this peak is caused solely by the axial flow deceleration.

With increasing radial offset from the center, as can be seen in Figs. 8(b)–8(d) and 8(f)–8(h) for offsets $1.5R_c$, $3.0R_c$, and $4.5R_c$, the influence of the shear components increases significantly. It can also be seen that the peak of the fluid stress is not only determined by the elongational flow components, but also partly by the shear component $\dot{S}_{xr} = \frac{1}{2} (\partial u_x / \partial r + \partial u_r / \partial x)$. This is further discussed in Sec. S2 of the Supplementary Material [64]. The radial offset at which the shear stress inside the nozzle channel exceeds the magnitude of the fluid stress peak depends on the shear thinning strength of the bioink: when comparing Figs. 8(c) and 8(g), the stress peak for the Newtonian fluid is already smaller than the fluid stress inside the nozzle channel, while for $\alpha = 0.75$, it is still higher. When selecting shear thinning bioinks in bioprinting, it is thus important to keep in mind that the relative significance of the radial flows at the nozzle exit, both elongational and corresponding shear components, increases when a stronger shear thinning bioink is used.

D. Cell flowing through the nozzle exit

In this section we investigate the influence of the flow transition on cells passing the exit of the printer nozzle using our computer simulations and actual micrographs of cells flowing through a real 3D bioprinter nozzle. As discussed in Sec. III C, elongational flow components on a short length scale ($\approx 2R$) occur at the nozzle exit. These act in different ways on the cell, depending on its radial position when passing the transition.

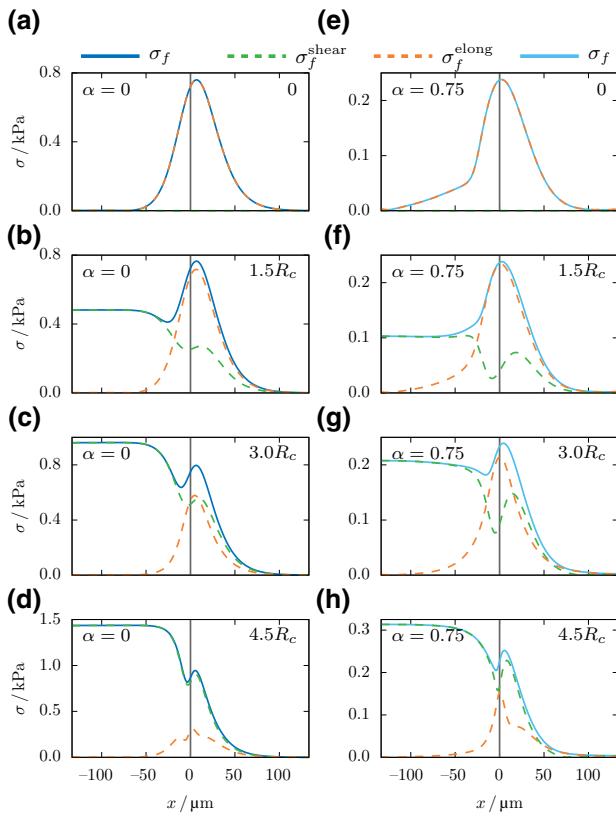


FIG. 8. Decomposition of the fluid stress in the shear, Eq. (13), and elongational component, Eq. (14), at the nozzle exit for the (a)–(d) Newtonian fluid and (e)–(h) the highly shear thinning bioink with $\alpha = 0.75$. Here x denotes the axial distance from the nozzle orifice.

1. Centered cell

Flowing along the center of the channel, the cell experiences symmetric flow conditions also when passing through the nozzle exit. The deceleration in flow direction leads to an axial compression, while the radial flow stretches the cell in the radial direction, leading to an oblate deformation of the cell. As can be seen in the simulation snapshots in Figs. 9(a) and 9(b) for the centered flowing cell, its stress uniformly increases inside the whole cell volume during this elongational deformation. After the transition, the cell quickly relaxes towards its spherical equilibrium shape inside the bioink strand.

Next, we assess the cellular stress resulting from the various flow regimes and ink properties that may affect cell survival and health. As can be seen in Fig. 10(a), an increase in the shear thinning strength of the bioink leads to a decreasing cell stress inside the nozzle channel, as expected from the experimentally observed increased cell survival in more shear thinning bioinks [22,45]. In contrast to these beneficial effects of shear thinning inside the nozzle, we find that the importance of the elongational stress peak at the nozzle exit notably increases relative to the

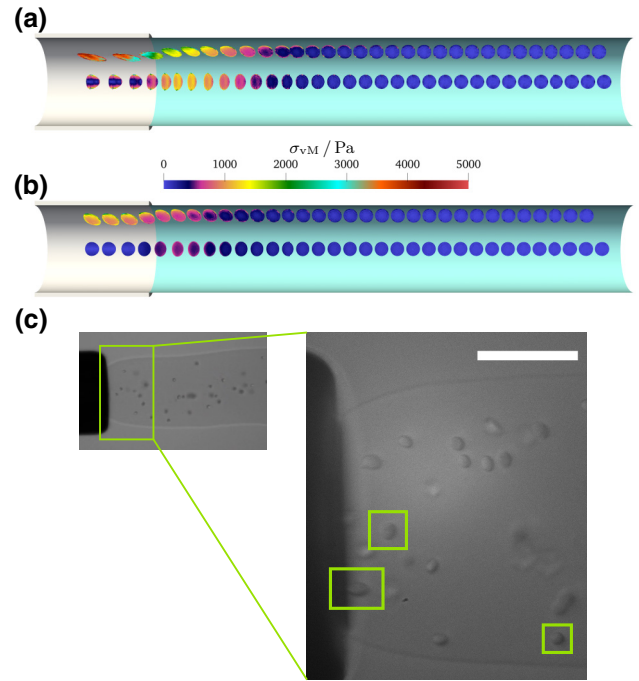


FIG. 9. Internal cell stress distribution of cells flowing at different offsets through the nozzle exit in (a) the Newtonian fluid and (b) the shear thinning bioink with $\alpha = 0.75$. (c) Experimental image of cells exiting a 100 μm radius nozzle in 2% alginate bioink. Left green boxes indicate radially (axially) elongated cells flowing in- (off-) center, respectively. The right green box indicates a cell after relaxation back to equilibrium. Movies of both the simulation and experiment can be found in the Supplementary Material.

stress inside the nozzle when α is increased: for the Newtonian case [dark blue line Fig. 10(a)], cell stress increases by approximately 50% from 0.9 to 1.3 kPa during the transition, while for the most shear thinning bioink (light blue line), it increases six fold from 0.1 to 0.6 kPa.

Besides cell stresses, an important measure to assess cell damage is cell strain; see, e.g., Ref. [14]. Because of the symmetry at the channel center, we define an axial strain $\alpha_1 := l_x/(2R_c)$ and a radial strain $\alpha_2 := l_r/(2R_c)$ as the maximum elongation of the cell in the considered direction divided by the cell's reference diameter. As shown in Fig. 11, the behavior of these cell strains is similar to that of the cell stresses in the paragraph above. Independent of the shear thinning exponent α , the axial strain α_1 of the cell's bullet shape inside the nozzle channel is almost negligible, and only a clear peak in deformation is observed when passing the nozzle exit. The radial strain α_2 , on the other hand, already starts with a significant difference from the equilibrium shape. A cell suspended in a highly shear thinning bioink flowing at the nozzle center therefore experiences only the elongational flow right at the nozzle exit, while remaining almost undeformed otherwise.

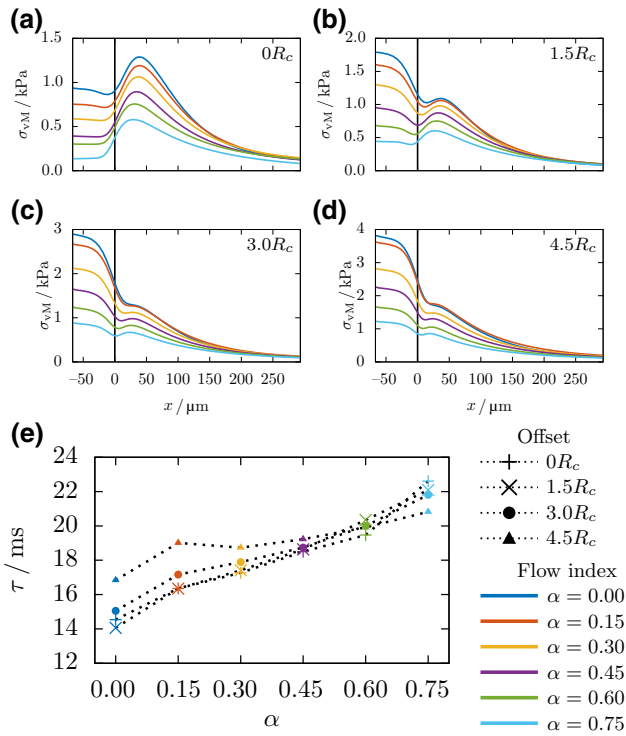


FIG. 10. Change of the cell stress when passing through the nozzle exit and flowing in the free bioink strand for increasingly shear thinning bioinks. From (a)–(d), the data are given for the initial cell’s radial offsets 0 , $1.5R_c$, $3R_c$, and $4.5R_c$. (e) Relaxation times τ of the cell stress when flowing in the free bioink strand as a function of α and the initial radial cell offset.

2. Off-centered cell

We now observe a cell flowing near the nozzle wall. Here, the elongational flow at the nozzle exit is combined with shear components inside the nozzle. When passing the transition, the cell is pushed in the radial direction leading to a nonellipsoidal change in shape, before it relaxes towards the equilibrium shape in the bioink strand. An overall decrease of the cell stress when passing through the transition can be observed in the simulation snapshots for the off-centered flowing cell in Figs. 9(a) and 9(b).

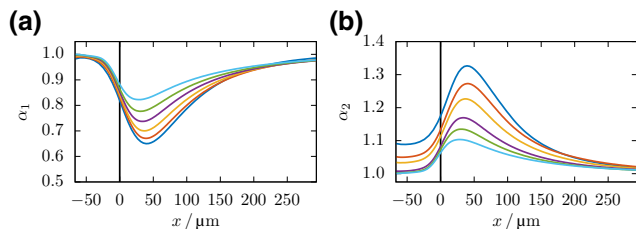


FIG. 11. Cell strain for a cell flowing in the center: (a) α_1 in the x direction and (b) α_2 in the r direction at the nozzle exit for the different bioinks. The colors correspond to the flow index as in Fig. 10.

Compared with centered cells in Fig. 10(a), the importance of elongational relative to shear stress decreases for off-centered cells as shown in Figs. 10(b)–10(d). Indeed, for off-centered cells, the relaxation from the shear-dominated axial flow inside the nozzle channel to the stress-free plug flow in the bioink strand is the most significant effect.

We determine this relaxation time scale τ for every simulation by fitting an exponentially decaying function to the cell stress versus time data (see Supplementary Material [64], Fig. S-8). Figure 10(e) shows the obtained relaxation times for all cell offsets as a function of α . We find that the relaxation time increases with increasing shear thinning strength α when keeping η_0 constant. This is caused by the larger viscosity of the bioinks with higher α for low rates of strain (cf. Fig. 1), resulting in a higher resistance of the fluid against the cell shape relaxation. Similar to our observations of the fluid stress at the nozzle exit in Sec. III C, we find in Figs. 10(a)–10(d) that the cell stress peak at the nozzle exit becomes more significant compared with the cell stress inside the nozzle channel when the cell is closer to the center and for stronger shear thinning fluids.

3. Microscopy experiments

To verify our numerical predictions, we use a high-speed camera to record images of a bioink strand with cells flowing out of a printing nozzle into a larger reservoir of water. Details of this imaging setup [74] are included in the Supplementary Material [64] (cf. Sec. S1). With the objective focused at the tip of the nozzle (inner radius $100 \mu\text{m}$), the micrograph in Fig. 9(c) shows cells suspended in a strand of 2% alginate bioink during extrusion at a flow rate of $10 \mu\text{l s}^{-1}$. As can be seen in the marked areas in Fig. 9(c), cells flowing close to the center exhibit a radially elongated change of shape, while cells flowing near the nozzle wall show an axial elongation. In accordance with our simulations, we observe the cells in the experiment relaxing towards their spherical stress-free shape shortly after the nozzle exit.

E. Prediction of elongational stress, cell stress, and cell strain during bioprinting

The methods employed in Secs. III B–III D lead to accurate predictions for important parameters such as cell strain or stress, but require numerical simulations with specialized software. As a practical tool, we develop in the following a simpler yet still accurate method to predict important cell quantities from the printing parameters only.

1. Elongational fluid stress at the nozzle exit

To quantify the importance of elongational effects, we define the average elongational fluid stress $\bar{\sigma}_f^{\text{elong}}$ that we obtain by averaging σ_f^{elong} from the simulations along the nozzle axis in an interval of $\mp R$ around the peak seen in

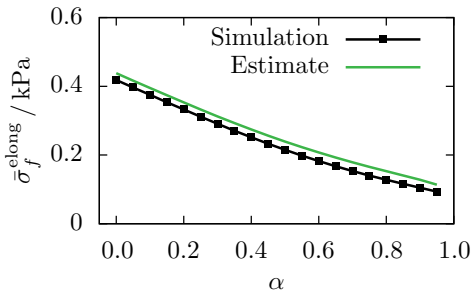


FIG. 12. Plot of the average elongational stress $\bar{\sigma}_f^{\text{elong}}$ across the nozzle exit from Figs. 8(a) and 8(e), estimated from Eq. (17).

Figs. 8(a) and 8(e). In Fig. 12 we plot $\bar{\sigma}_f^{\text{elong}}$ as a function of the shear thinning strength of the fluid. As would be expected from the decreasing pressure gradient, the elongational stress monotonously decreases with α . In order to obviate the need for full numerical simulations of the entire flow field in practice, we now show that a good estimate for $\bar{\sigma}_f^{\text{elong}}$ can be obtained by using a much simpler method for flow-field computations [42].

For this, we assume that the length of the transition is equal to the nozzle diameter $2R$, as can be verified by comparing with Figs. 7(a) and 7(b) and 8(a) and 8(e). Starting from the velocity profile of Ref. [42], the change in axial velocity along this length then gives the approximate elongation rate at the nozzle exit,

$$\dot{\epsilon} \approx \frac{u_x^{\text{max}} - u_x^{\text{avg}}}{2R}. \quad (16)$$

Next, we calculate the stress assuming elongational flow conditions, i.e., $\dot{S}_{xx} = -2\dot{S}_{rr} = -2\dot{S}_{\theta\theta} = -\dot{\epsilon}$, via

$$\bar{\sigma}_f^{\text{elong}} = \eta \left(\sqrt{3}\dot{\epsilon} \right) \sqrt{3}\dot{\epsilon}, \quad (17)$$

which is derived in the Supplementary Material [64] (cf. Sec. S3). This approximated average elongational stress is in very good agreement with the full numerical simulation of the nozzle exit, as shown in Fig. 12.

We use this approximation to further estimate the elongational cell strain and stress for centered flowing cells at the nozzle exit in the next section.

2. Cell stress and strain for centered cells

We proceed with an estimation of the maximum stress and strain experienced by cells while flowing inside the nozzle as well as during their transition into the free strand at the nozzle exit.

Starting with the latter, we focus on cells flowing at or close to the nozzle center where (as we show in Figs. 8(a), 8(b), 8(e), and 8(f) above) elongational stresses are the most significant fluid stress contribution. The theories of

Jeffery and Roscoe [49,50] contain a solution for the cell strains α_1 and α_2 in a stationary elongational flow (cf. Sec. S4 B of the Supplementary Material [64]). It reads

$$\frac{2}{\sqrt{3}} \frac{\bar{\sigma}_f^{\text{elong}}}{\mu} = \left(\alpha_1^2 - \frac{1}{\alpha_1} \right) \int_0^\infty \frac{\lambda d\lambda}{\left(\frac{1}{\alpha_1} + \lambda \right)^2 (\alpha_1^2 + \lambda)^{3/2}} \quad (18)$$

and can be solved numerically for α_1 as a function of the elongational fluid stress and the cell's shear modulus. The other cell strains are $\alpha_2 = \alpha_3 = \alpha_1^{-1/2}$ due to symmetry. Using the elongation rate from Eq. (17) as an input value, we compare the theoretical values with the data obtained from the full numerical simulations in Fig. 13(a). We note that the theory slightly, but consistently, overestimates cell strains. Indeed, since the elongational flow is experienced by the cell for only a short time span while the theory assumes a stationary elongational flow, this overestimation is to be expected. Interestingly, and in line with what has already been observed in Fig. 6, Roscoe theory yields surprisingly accurate predictions even for highly shear thinning inks. We again attribute this to the central role of stresses, instead of flow rates, for the cell deformation process in printing nozzles when these are large compared with the radius of the cell. With our approximation consistently overestimating the simulated results, it can be considered as a practical upper limit for predicting cell survival.

As a consequence of the stationarity condition assumed by Roscoe theory, it would predict unrealistically large cell strains in the case of printing velocities higher than the 0.5 mm s^{-1} used in this work. In reality, however, the flow through the nozzle exit is highly transient and the stationary state is never attained. To assess nevertheless the effect of printing speed, we perform additional simulations for cells flowing centered through the nozzle at $1\text{--}10 \text{ cm s}^{-1}$ average extrusion velocity, in order to cover the typical range of 3D bioprinting speeds. Figure 14(a) shows the resulting peak cell strains at the exit from full numerical simulations in comparison to our estimate for 0.5 mm s^{-1} in Fig. 13(a). It is apparent that a variation of more than one order of magnitude in flow velocity hardly affects the cell strains, since the higher velocities significantly decrease the time span during which the high elongational stresses are acting on the cell. Hence, the printing speed does not practically affect the elongational strains occurring during printing.

Based on this estimate for cell strain, we proceed to estimate the corresponding cell stress for centered cells. For this, the fluid elongational stress from Eq. (17) is fed into the elongational Roscoe theory given by Eq. (18) and Eq. (S-52) in the Supplementary Material [64]. The result is in good agreement with the full numerical simulations as shown in Fig. 13(b) for centered cells (green line).

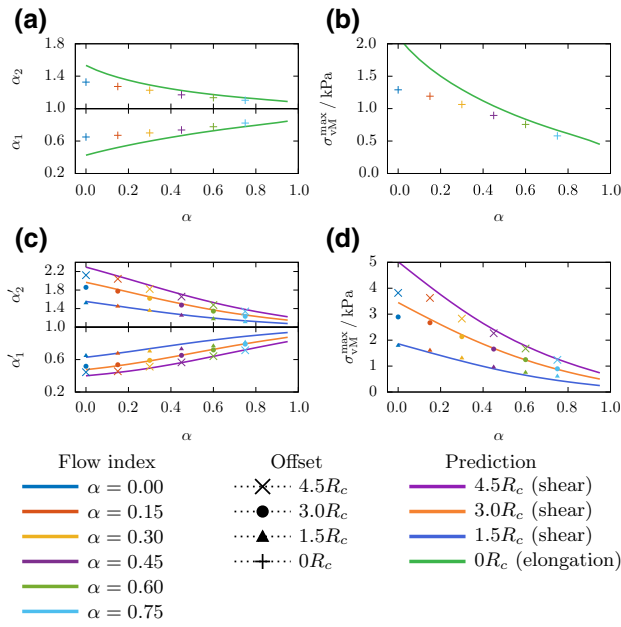


FIG. 13. (a) The peak strain and (b) cell stress for centered flowing cells at the transition can be approximated using our estimate of the average elongational fluid stress from Eq. (17) and the Jeffery and Roscoe theories for a cell in an elongational flow from Sec. S4 B of the Supplementary Material [64]. For off-centered cells, our flow calculations inside the nozzle channel and the theory of Roscoe for a cell in shear flow. (c) and (d) For off-centered cells, our flow calculations inside the nozzle channel and the theory of Roscoe for a cell in shear flow are in good agreement.

3. Cell stress and strain for off-centered cells

For off-centered cells, we show in Fig. 10(d) that shear components inside the nozzle are an important contribution to the overall cell stress, especially inside less shear

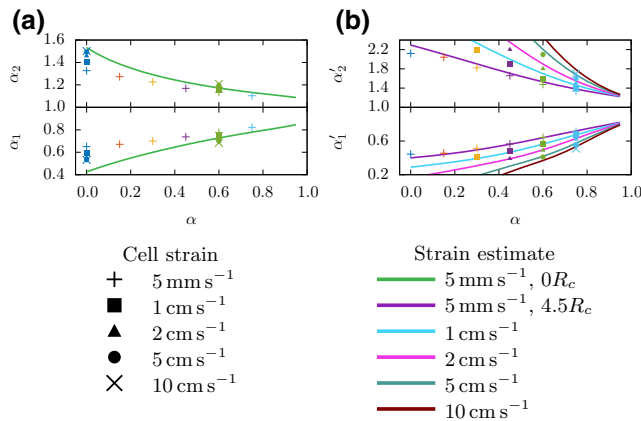


FIG. 14. (a) Peak elongational cell strain for centered flowing cells passing the transition for an average extrusion velocity of 1, 2, 5, and 10 cm s^{-1} in comparison to the data of Fig. 13(a) for 5 mm s^{-1} . (b) Maximum cell strain for cells flowing off-centered at $4.5 R_c$ for increasing velocities is in accordance with the prediction of the Roscoe theory.

thinning bioinks, where they substantially exceed the stress caused by elongational flows at the nozzle exit. Next we estimate this overall maximum cell strain and stress.

Because of their almost ellipsoidal shape, we now choose as a strain measure for the off-centered flowing cells the ellipsoid's major and minor semiaxis α'_1 and α'_2 , which are obtained through computing the equivalent ellipsoid from the deformed cell's inertia tensor, as detailed in Ref. [31].

Starting from the fluid shear stress obtained from our earlier work [42], we employ the shear part of Roscoe theory in Eqs. (S-45) and (S-47) of the Supplementary Material [64] and plot the resulting stresses and strains for cells starting at $1.5R_c$, $3R_c$, and $4.5R_c$ in Figs. 13(c) and 13(d). Again, we observe very good agreement with the simulations from Sec. III D(ii).

Upon increasing the average flow velocity by more than one order of magnitude in Fig. 14(b), we find that cells flowing at maximum radial offset in Newtonian bioinks are not able to attain a stable state while flowing inside the nozzle channel. However, this limitation is solely a result of the large viscosity of the hypothetical Newtonian fluid, and would not affect a real printing process. With increasing shear thinning strength, as shown in Fig. 14(b), a stable cell shape can be achieved also for high flow velocities of 10 cm s^{-1} . The maximum cell strains are accurately predicted by Roscoe theory.

IV. CONCLUSION

In this work we investigate the cell stress and strain and the bioink flow behavior during a 3D bioprinting extrusion process using lattice Boltzmann numerical simulations together with corresponding qualitative experiments. The two scenarios considered are the flow inside the nozzle channel as well as at the nozzle exit, where the flow transitions into the free bioink strand.

During the first stage of the printing process while cells are flowing inside the printing nozzle, our simulations show a bulletlike deformation for cells in the center of the channel and an ellipsoidal shape for cells flowing off-center. The latter can be understood on the basis of the classical theory of Roscoe [50] that relates cell stress to the local fluid stress. Interestingly, our simulations demonstrate that these relations hold even in realistic shear thinning bioinks, even though they were originally designed for Newtonian fluids only. The radially inward-directed migration of the cell due to the shear forces is also found to be independent of the shear thinning strength and solely dependent on the printing pressure. We show that, when bioprinting at a constant flow rate (or velocity), the shear thinning properties reduce the overall cell stress and strain significantly, while this is not the case for printing processes performed at constant printing pressure.

In the second stage cells transition into the free printing strand as they exit the printer nozzle. During this transition, cells are exposed to an elongational flow pattern. While a radial deformation also occurs for cells flowing off-center, we find that the shear deformations dominate in this case. For cells in the channel center, however, this flow causes a notable radial stretch of the cells as predicted by our numerical simulations, in qualitative agreement with experimental microscopy images. We show that this effect becomes particularly relevant for cells flowing in highly shear thinning bioinks, as the shear deformation inside the nozzle can virtually be eliminated, while the radial elongation inevitably takes place [Fig. 10(a)]. In addition, we find that the elongational cell strain is practically independent of the extrusion velocity of the bioink, since the faster velocity balances the high elongational stress by reducing the application time. The relaxation times of the elongated cells even increase with the shear thinning strength, thus prolonging the time that they remain under strain with potentially harmful side effects [Fig. 10(e)].

Using our numerical simulation techniques as a starting point together with the velocity profiles derived in our earlier work [42], we finally develop simple estimates for cell stress and/or cell strain for centered as well as off-centered cells.

ACKNOWLEDGMENTS

We thank Nico Schwarm for preparing the cell and alginate samples and for helping with the imaging experiment. Funded by the Deutsche Forschungsgemeinschaft (DFG, German Research Foundation)—Project No. 326998133—TRR 225 “Biofabrication” (subprojects B07 and A01). We gratefully acknowledge computing time provided by the SuperMUC system of the Leibniz Rechenzentrum, Garching. We further acknowledge support through the computational resources provided by the Bavarian Polymer Institute.

- [1] W. Sun, B. Starly, A. C. Daly, J. A. Burdick, J. Groll, G. Skeldon, W. Shu, Y. Sakai, M. Shinohara, M. Nishikawa, J. Jang, D.-W. Cho, M. Nie, S. Takeuchi, S. Ostrovidov, A. Khademhosseini, R. D. Kamm, V. Mironov, L. Moroni, and I. T. Ozbolat, The bioprinting roadmap, *Biofabrication* **12**, 022002 (2020).
- [2] R. W. Barrs, J. Jia, S. E. Silver, M. Yost, and Y. Mei, Biomaterials for bioprinting microvasculature, *Chem. Rev.* **120**, 10887 (2020).
- [3] R. Levato, T. Jungst, R. G. Scheuring, T. Blunk, J. Groll, and J. Malda, From shape to function: The next step in bioprinting, *Adv. Mater.* **32**, 1906423 (2020).
- [4] J. Groll, T. Boland, T. Blunk, J. A. Burdick, D.-W. Cho, P. D. Dalton, B. Derby, G. Forgacs, Q. Li, V. A. Mironov, L. Moroni, M. Nakamura, W. Shu, S. Takeuchi, G. Vozzi, T.

- B. F. Woodfield, T. Xu, J. J. Yoo, and J. Malda, Biofabrication: Reappraising the definition of an evolving field, *Biofabrication* **8**, 013001 (2016).
- [5] J. Malda, J. Visser, F. P. Melchels, T. Jungst, W. E. Hennink, W. J. A. Dhert, J. Groll, and D. W. Huttmacher, 25th anniversary article: Engineering hydrogels for biofabrication, *Adv. Mater.* **25**, 5011 (2013).
- [6] T. Böck, V. Schill, M. Krähnke, A. F. Steinert, J. Tessmar, T. Blunk, and J. Groll, TGF- β 1-modified hyaluronic acid/poly(glycidol) hydrogels for chondrogenic differentiation of human mesenchymal stromal cells, *Macromol. Biosci.* **18**, 1700390 (2018).
- [7] T. U. Esser, K. Roshanbinfar, and F. B. Engel, Promoting vascularization for tissue engineering constructs: Current strategies focusing on HIF-regulating scaffolds, *Expert Opin. Biol. Ther.* **19**, 105 (2019).
- [8] J. Hauptstein, T. Böck, M. Bartolf-Kopp, L. Forster, P. Stahlhut, A. Nadernezhad, G. Blahetek, A. Zernecke-Madsen, R. Detsch, T. Jungst, J. Groll, J. Teßmar, and T. Blunk, Hyaluronic acid-based bioink composition enabling 3D bioprinting and improving quality of deposited cartilaginous extracellular matrix, *Adv. Healthc. Mater.* **9**, 2000737 (2020).
- [9] I. A. D. Mancini, S. Schmidt, H. Brommer, B. Pouran, S. Schäfer, J. Tessmar, A. Mensinga, M. H. P. van Rijen, J. Groll, T. Blunk, R. Levato, J. Malda, and P. R. van Weeren, A composite hydrogel-3D printed thermoplast osteochondral anchor as example for a zonal approach to cartilage repair: *In vivo* performance in a long-term equine model, *Biofabrication* **12**, 035028 (2020).
- [10] C. Mueller, M. Trujillo-Miranda, M. Maier, D. E. Heath, A. J. O'Connor, and S. Salehi, Effects of external stimulators on engineered skeletal muscle tissue maturation, *Adv. Mater. Interfaces* **8**, 2001167 (2021).
- [11] K. Roshanbinfar, L. Vogt, B. Greber, S. Diecke, A. R. Boccaccini, T. Scheibel, and F. B. Engel, Electroconductive biohybrid hydrogel for enhanced maturation and beating properties of engineered cardiac tissues, *Adv. Funct. Mater.* **28**, 1803951 (2018).
- [12] S. Schmidt, F. Abinzano, A. Mensinga, J. Teßmar, J. Groll, J. Malda, R. Levato, and T. Blunk, Differential production of cartilage ECM in 3D agarose constructs by equine articular cartilage progenitor cells and mesenchymal stromal cells, *Int. J. Mol. Sci.* **21**, 7071 (2020).
- [13] A. Weizel, T. Distler, D. Schneidereit, O. Friedrich, L. Bräuer, F. Paulsen, R. Detsch, A. Boccaccini, S. Budday, and H. Seitz, Complex mechanical behavior of human articular cartilage and hydrogels for cartilage repair, *Acta Biomater.* **118**, 113 (2020).
- [14] L. Fischer, M. Nosratlo, K. Hast, E. Karakaya, N. Ströhlein, T. U. Esser, R. Gerum, S. Richter, F. Engel, R. Detsch, B. Fabry, and I. Thievensen, Calcium supplementation of bioinks reduces shear stress-induced cell damage during bioprinting, *Biofabrication* **14**, 045005 (2022).
- [15] S. Han, C. M. Kim, S. Jin, and T. Y. Kim, Study of the process-induced cell damage in forced extrusion bioprinting, *Biofabrication* **13**, 035048 (2021).
- [16] G. Poologasundarampillai, A. Haweet, S. N. Jayash, G. Morgan, J. E. Moore, and A. Candeo, Real-time imaging and analysis of cell-hydrogel interplay within an extrusion-bioprinting capillary, *Bioprinting* **23**, e00144 (2021).

- [17] J. Emmermacher, D. Spura, J. Cziommer, D. Kilian, T. Wollborn, U. Fritsching, J. Steingroewer, T. Walther, M. Gelinsky, and A. Lode, Engineering considerations on extrusion-based bioprinting: Interactions of material behavior, mechanical forces and cells in the printing needle, *Biofabrication* **12**, 025022 (2020).
- [18] S. Boularaoui, G. Al Hussein, K. A. Khan, N. Christoforou, and C. Stefanini, An overview of extrusion-based bioprinting with a focus on induced shear stress and its effect on cell viability, *Bioprinting* **20**, e00093 (2020).
- [19] F. Ruther, T. Distler, A. R. Boccaccini, and R. Detsch, Biofabrication of vessel-like structures with alginate dialdehyde—gelatin (ADA-GEL) bioink, *J. Mater. Sci.: Mater. Med.* **30**, 8 (2019).
- [20] J. Shi, B. Wu, S. Li, J. Song, B. Song, and W. F. Lu, Shear stress analysis and its effects on cell viability and cell proliferation in drop-on-demand bioprinting, *Biomed. Phys. Eng. Exp.* **4**, 045028 (2018).
- [21] N. Paxton, W. Smolan, T. Böck, F. Melchels, J. Groll, and T. Jungst, Proposal to assess printability of bioinks for extrusion-based bioprinting and evaluation of rheological properties governing bioprintability, *Biofabrication* **9**, 044107 (2017).
- [22] L. Ouyang, R. Yao, Y. Zhao, and W. Sun, Effect of bioink properties on printability and cell viability for 3D bioplotting of embryonic stem cells, *Biofabrication* **8**, 035020 (2016).
- [23] A. Blaeser, D. F. Duarte Campos, U. Puster, W. Richtering, M. M. Stevens, and H. Fischer, Controlling shear stress in 3D bioprinting is a key factor to balance printing resolution and stem cell integrity, *Adv. Healthc. Mater.* **5**, 326 (2015).
- [24] J. Snyder, A. Rin Son, Q. Hamid, C. Wang, Y. Lui, and W. Sun, Mesenchymal stem cell printing and process regulated cell properties, *Biofabrication* **7**, 044106 (2015).
- [25] Y. Zhao, Y. Li, S. Mao, W. Sun, and R. Yao, The influence of printing parameters on cell survival rate and printability in microextrusion-based 3D cell printing technology, *Biofabrication* **7**, 045002 (2015).
- [26] J. Hazur, R. Detsch, E. Karakaya, J. Kaschta, J. Teßmar, D. Schneiderit, O. Friedrich, D. W. Schubert, and A. R. Boccaccini, Improving alginate printability for biofabrication: Establishment of a universal and homogeneous pre-crosslinking technique, *Biofabrication* **12**, 045004 (2020).
- [27] C. Hu, L. Hahn, M. Yang, A. Altmann, P. Stahlhut, J. Groll, and R. Luxenhofer, Improving printability of a thermoresponsive hydrogel biomaterial ink by nanoclay addition, *J. Mater. Sci.* **56**, 691 (2021).
- [28] A. Nadernezhad, L. Forster, F. Netti, L. Adler-Abramovich, J. Teßmar, and J. Groll, Rheological analysis of the interplay between the molecular weight and concentration of hyaluronic acid in formulations of supramolecular HA/FmocFF hybrid hydrogels, *Polym. J.* **52**, 1007 (2020).
- [29] M. Weis, J. Shan, M. Kuhlmann, T. Jungst, J. Tessmar, and J. Groll, Evaluation of hydrogels based on oxidized hyaluronic acid for bioprinting, *Gels* **4**, 82 (2018).
- [30] P. K. Sanagavarapu, G. Subramanian, and P. R. Nott, Shape dynamics and rheology of dilute suspensions of elastic and viscoelastic particles, *J. Fluid Mech.* **949**, A22 (2022).
- [31] S. J. Müller, F. Weigl, C. Bezold, C. Bächer, K. Albrecht, and S. Gekle, A hyperelastic model for simulating cells in flow, *Biomech. Model. Mechanobiol.* **20**, 509 (2021).
- [32] B. Fregin, F. Czerwinski, D. Biedenweg, S. Girardo, S. Gross, K. Aurich, and O. Otto, High-throughput single-cell rheology in complex samples by dynamic real-time deformability cytometry, *Nat. Commun.* **10**, 415 (2019).
- [33] A. Saadat, C. J. Guido, G. Iaccarino, and E. S. G. Shaqfeh, Immersed-finite-element method for deformable particle suspensions in viscous and viscoelastic media, *Phys. Rev. E* **98**, 063316 (2018).
- [34] M. Mokbel, D. Mokbel, A. Mietke, N. Träber, S. Girardo, O. Otto, J. Guck, and S. Aland, Numerical simulation of real-time deformability cytometry to extract cell mechanical properties, *ACS Biomater. Sci. Eng.* **3**, 2962 (2017).
- [35] A. Mietke, O. Otto, S. Girardo, P. Rosendahl, A. Taubenberger, S. Golfier, E. Ulbricht, S. Aland, J. Guck, and E. Fischer-Friedrich, Extracting cell stiffness from real-time deformability cytometry: Theory and experiment, *Biophys. J.* **109**, 2023 (2015).
- [36] O. Otto, P. Rosendahl, A. Mietke, S. Golfier, C. Herold, D. Klaue, S. Girardo, S. Pagliara, A. Ekpenyong, A. Jacobi, M. Wobus, N. Töpfner, U. F. Keyser, J. Mansfeld, E. Fischer-Friedrich, and J. Guck, Real-time deformability cytometry: On-the-fly cell mechanical phenotyping, *Nat. Methods* **12**, 199 (2015).
- [37] F. Huber, J. Schnauß, S. Rönicke, P. Rauch, K. Müller, C. Fütterer, and J. Käs, Emergent complexity of the cytoskeleton: From single filaments to tissue, *Adv. Phys.* **62**, 1 (2013).
- [38] M. L. Rodriguez, P. J. McGarry, and N. J. Sniadecki, Review on cell mechanics: Experimental and modeling approaches, *Appl. Mech. Rev.* **65**, 060801 (2013).
- [39] T. Gao, H. H. Hu, and P. P. Castañeda, Rheology of a suspension of elastic particles in a viscous shear flow, *J. Fluid Mech.* **687**, 209 (2011).
- [40] P. Kollmannsberger and B. Fabry, Linear and nonlinear rheology of living cells, *Annu. Rev. Mater. Res.* **41**, 75 (2011).
- [41] L. Ning, N. Betancourt, D. J. Schreyer, and X. Chen, Characterization of cell damage and proliferative ability during and after bioprinting, *ACS Biomater. Sci. Eng.* **4**, 3906 (2018).
- [42] S. J. Müller, E. Mirzahosseini, E. N. Iftexhar, C. Bächer, S. Schrüfer, D. W. Schubert, B. Fabry, and S. Gekle, Flow and hydrodynamic shear stress inside a printing needle during biofabrication, *PLoS ONE* **15**, e0236371 (2020).
- [43] L. Lemarié, A. Anandan, E. Petiot, C. Marquette, and E.-J. Courtial, Rheology, simulation and data analysis toward bioprinting cell viability awareness, *Bioprinting* **21**, e00119 (2021).
- [44] K. Fakhruddin, M. S. A. Hamzah, and S. I. A. Razak, Effects of extrusion pressure and printing speed of 3D bioprinted construct on the fibroblast cells viability, *IOP Conf. Ser.: Mater. Sci. Eng.* **440**, 012042 (2018).
- [45] T. Billiet, E. Gevaert, T. De Schryver, M. Cornelissen, and P. Dubruel, The 3D printing of gelatin methacrylamide cell-laden tissue-engineered constructs with high cell viability, *Biomaterials* **35**, 49 (2014).
- [46] Y. B. Bae, H. K. Jang, T. H. Shin, G. Phukan, T. T. Tran, G. Lee, W. R. Hwang, and J. M. Kim, Microfluidic assessment of mechanical cell damage by extensional stress, *Lab Chip* **16**, 96 (2016).

- [47] K. Nair, M. Gandhi, S. Khalil, K. C. Yan, M. Marcolongo, K. Barbee, and W. Sun, Characterization of cell viability during bioprinting processes, *Biotechnol. J.* **4**, 1168 (2009).
- [48] R. Chang, J. Nam, and W. Sun, Effects of dispensing pressure and nozzle diameter on cell survival from solid freeform fabrication-based direct cell writing, *Tissue Eng. Part A* **14**, 41 (2008).
- [49] G. B. Jeffery, The motion of ellipsoidal particles immersed in a viscous fluid, *Proc. R. Soc. London Ser. A, Containing Pap. Math. Phys. Charact.* **102**, 161 (1922).
- [50] R. Roscoe, On the rheology of a suspension of viscoelastic spheres in a viscous liquid, *J. Fluid Mech.* **28**, 273 (1967).
- [51] T. Krüger, H. Kusumaatmaja, A. Kuzmin, O. Shardt, G. Silva, and E. M. Viggien, *The Lattice Boltzmann Method, Graduate Texts in Physics* (Springer International Publishing, Cham, 2017).
- [52] M. Lehmann, M. J. Krause, G. Amati, M. Sega, J. Harting, and S. Gekle, Accuracy and performance of the lattice Boltzmann method with 64-bit, 32-bit, and customized 16-bit number formats, *Phys. Rev. E* **106**, 015308 (2022).
- [53] H. Limbach, A. Arnold, B. Mann, and C. Holm, ESPResSo—an extensible simulation package for research on soft matter systems, *Comput. Phys. Commun.* **174**, 704 (2006).
- [54] D. Roehm and A. Arnold, Lattice Boltzmann simulations on GPUs with ESPResSo, *Eur. Phys. J. Spec. Top.* **210**, 89 (2012).
- [55] M. Schlenk, E. Hofmann, S. Seibt, S. Rosenfeldt, L. Schrack, M. Drechsler, A. Rothkirch, W. Ohm, J. Breu, S. Gekle, and S. Förster, Parallel and perpendicular alignment of anisotropic particles in free liquid microjets and emerging microdroplets, *Langmuir* **34**, 4843 (2018).
- [56] D. Devendran and C. S. Peskin, An immersed boundary energy-based method for incompressible viscoelasticity, *J. Comput. Phys.* **231**, 4613 (2012).
- [57] C. Bächer, L. Schrack, and S. Gekle, Clustering of microscopic particles in constricted blood flow, *Phys. Rev. Fluids* **2**, 013102 (2017).
- [58] C. Bächer and S. Gekle, Computational modeling of active deformable membranes embedded in three-dimensional flows, *Phys. Rev. E* **99**, 062418 (2019).
- [59] M. M. Cross, Rheology of non-Newtonian fluids: A new flow equation for pseudoplastic systems, *J. Colloid Sci.* **20**, 417 (1965).
- [60] V. Manojlovic, J. Djonlagic, B. Obradovic, V. Nedovic, and B. Bugarski, Investigations of cell immobilization in alginate: Rheological and electrostatic extrusion studies, *J. Chem. Technol. Biotechnol.* **81**, 505 (2006).
- [61] Or using our web tool under <https://bio.physik.fau.de/flow/webpage/flow.html>.
- [62] M. E. Rosti, L. Brandt, and D. Mitra, Rheology of suspensions of viscoelastic spheres: Deformability as an effective volume fraction, *Phys. Rev. Fluids* **3**, 012301 (2018).
- [63] A. F. Bower, *Applied Mechanics of Solids* (CRC Press, Boca Raton, 2010).
- [64] See Supplemental Material at <http://link.aps.org/supplemental/10.1103/PhysRevApplied.19.064061>.
- [65] R. Kiss, Elasticity of human embryonic stem cells as determined by atomic force microscopy, *J. Biomech. Eng.* **133**, 101009 (2011).
- [66] C. Geuzaine and J.-F. Remacle, Gmsh: A 3-D finite element mesh generator with built-in pre- and post-processing facilities, *Int. J. Numer. Methods Eng.* **79**, 1309 (2009).
- [67] R. Mittal and G. Iaccarino, Immersed boundary methods, *Annu. Rev. Fluid Mech.* **37**, 239 (2005).
- [68] C. S. Peskin, The immersed boundary method, *Acta Numer.* **11**, 479 (2002).
- [69] Z. Chai, B. Shi, Z. Guo, and F. Rong, Multiple-relaxation-time lattice Boltzmann model for generalized Newtonian fluid flows, *J. Nonnewton. Fluid Mech.* **166**, 332 (2011).
- [70] M. Lehmann, S. J. Müller, and S. Gekle, Efficient viscosity contrast calculation for blood flow simulations using the lattice Boltzmann method: Efficient viscosity contrast calculation for blood flow simulations using the lattice Boltzmann method, *Int. J. Numer. Methods Fluids* **92**, 1463 (2020).
- [71] P. Fisch, M. Holub, and M. Zenobi-Wong, Improved accuracy and precision of bioprinting through progressive cavity pump-controlled extrusion, *Biofabrication* **13**, 015012 (2021).
- [72] R. Gerum, *et al.*, Viscoelastic properties of suspended cells measured with shear flow deformation cytometry, *eLife* **11**, e78823 (2022).
- [73] E. Guazzelli, J. F. Morris, and S. Pic, *A Physical Introduction to Suspension Dynamics, Cambridge Texts in Applied Mathematics* (Cambridge University Press, Cambridge; New York, 2012).
- [74] M. Kahl, M. Gertig, P. Hoyer, O. Friedrich, and D. F. Gilbert, Ultra-low-cost 3D bioprinting: Modification and application of an off-the-shelf desktop 3D-printer for biofabrication, *Front. Bioeng. Biotechnol.* **7**, 184 (2019).